# Ferruginous oceans during OAE1a and the collapse of the seawater sulphate reservoir

Kohen W. Bauer[1,2,‡], Cinzia Bottini[3], Sergei Katsev[4], Mark Jellinek[1], Roger Francois[1], Elisabetta Erba[3], Sean A. Crowe[1,2, ‡*]

[1]Department of Earth, Ocean and Atmospheric Sciences,
The University of British Columbia, 2020 - 2207 Main Mall,
Vancouver, British Columbia V6T 1Z4, Canada

[2]Department of Microbiology and Immunology, Life Sciences Centre,
The University of British Columbia, 2350 Health Sciences Mall,
Vancouver, British Columbia, V6T 1Z3, Canada

[3]Department of Earth Sciences,
University of Milan, Via Mangiagalli 34,
20133 Milan, Italy

[4]Large Lakes Observatory and Department of Physics
University of Duluth, 2205 E 5th St,
Duluth, Minnesota, 55812, USA

*Corresponding author; sean.crowe@ubc.ca

[‡]Current address; Department of Earth Sciences
University of Hong Kong
Pokfulam Road, Hong Kong SAR

**At 28 mM seawater sulphate is one of the largest oxidant pools at Earth's surface and its concentration in the oceans is generally assumed to have remained above 5 mM since the early Phanerozoic (400 Ma). Intermittent and potentially global oceanic anoxic events (OAEs) are accompanied by changes in seawater sulphate concentrations and signal perturbations in the Earth system associated with major climatic anomalies and biological crises. Ferruginous (Fe-rich) ocean conditions developed transiently during multiple OAEs, implying strong variability in seawater chemistry and global biogeochemical cycles. The precise evolution of seawater sulphate concentrations during OAEs remains uncertain and thus models that aim to mechanistically link ocean anoxia to broad-scale disruptions in the Earth system remain largely equivocal. Here we show that during OAE1a, 125 Ma, the oceans were anoxic and ferruginous for more than 1 million years. Development of ferruginous conditions at this time requires low seawater sulphate concentrations, which likely dropped to < 70 μM or more than a hundred times lower than modern. This collapse in the seawater sulphate pool over just a few hundred thousand years or less, reveals previously unrecognized dynamics in Phanerozoic Earth surface redox budgets with potential to dramatically alter global biogeochemical cycles, marine biology, and climate on remarkably short time-scales.**

Seawater chemistry is generally thought to have evolved to its current well-oxygenated, sulphate-rich state between 540 and 420 million years ago (Ma) [1, 2]. Throughout much of the preceding 3.5 billion years, the oceans were largely anoxic, predominantly Fe-rich (ferruginous), and punctuated by intervals of widespread hydrogen sulphide-rich conditions (euxinic) [3, 4]. These conditions waned in the early Phanerozoic, and thus, for much of the last 500 Myr, marine and global biogeochemical cycles were thought to have operated much as they do today [5, 6]. Large-scale oceanic anoxic conditions, however, re-emerged intermittently in the Phanerozoic Eon [7] and were particularly prevalent during warm periods such as the Cretaceous. The oceans developed euxinia during a number of these oceanic anoxic events (OAEs) [8, 9] when pelagic microbial respiration was channelled through sulphate reduction producing hydrogen sulphide that accumulated in poorly ventilated water masses. Emerging evidence, however, also suggests that transient ferruginous conditions occurred during several of the OAEs (OAE2, OAE3 and the end-Permian OAE) [8, 10, 11]. Since development of ferruginous conditions hinges on the balance between Fe and S delivery and removal from the oceans [4], such temporal dynamics imply large-scale variability in ocean chemistry and the S cycle.

Sulphur isotope signals and fluid inclusion data recorded during the Cretaceous Period reveal that background seawater sulphate concentrations were much lower (5 – 10 mM) [12, 13, 14, 15, 16] than the modern ocean (28 mM). Episodic evaporite deposition likely drew down seawater sulphate concentrations even further (possibly to as low as 1 mM), during the early Cretaceous [17]. This evaporite deposition likely took place intermittently both before [18, 19], and after [20] Aptian OAE1a (~125 Ma). Some stratigraphic reconstructions imply evaporite deposition contemporaneous with OAE1a [21], however, this timing is not well supported by independent chronostratigraphic data.

Low seawater sulphate concentrations could have strongly influenced global biogeochemical cycling. For example, seawater sulphate concentrations are an important control on marine methane ($CH_4$) cycling, with super-millimolar sulphate concentrations attenuating the release of $CH_4$ generated in modern marine sediments to the atmosphere through microbial anaerobic methane oxidation [22, 23]. Sub-millimolar sulphate concentrations, in contrast, can lead to large-scale oceanic $CH_4$ efflux with corresponding implications for climate [24]. While S-isotope data imply low mM sulphate concentrations [13, 14, 15, 17], existing models and data lack the resolution needed to place robust upper limits on possible marine sulphate concentrations that would facilitate reconstruction of the climate system and the effects of OAE development on the biosphere.

To constrain seawater sulphate concentrations in the early Cretaceous, we studied a suite of sedimentary rocks from the eastern margin of the Paleo-Tethys Ocean (Cismon drill core) and the middle of the Paleo-Panthalassic Ocean (Deep Sea Drilling Project (DSDP) Site 463) that capture OAE1a. This interval is delineated by the deposition of organic matter (OM)-rich black shale containing units for more than a million years [25, 26]. We analysed rocks from OAE1a using selective sequential extractions to partition Fe speciation between operationally defined phases (Supplementary Information), and distinguish between Fe burial as pyrite and other forms of reactive Fe (i.e. non-lithogenic). These sequential extractions target Fe-phases considered highly reactive ($Fe_{HR}$ = sum of all non-silicate Fe) towards sulphide (pyritization) and biological and abiological Fe(III) reduction under anoxic conditions [27, 28, 29]. Fe-speciation analyses thus enable us to discriminate between sediments deposited under anoxic ferruginous versus euxinic water column states, based on the degree of pyritization of this $Fe_{HR}$ pool [4, 29]. Notably, preservation of $Fe_{HR}$ in sediments that also contain appreciable organic matter implies that pyritization was sulphate limited [30].

## Ferruginous conditions during OAE1a

OAE1a is characterized by a C-isotope excursion as well as by deposition of OM-rich sediment, which are evident between ~18-24 m in the Cismon core and ~615-625 m in DSDP Site 463 (Fig. 1). Our Fe-speciation analyses reveal enrichments of pyritizable Fe ($Fe_{HR}$) across these same intervals in both Cismon and DSDP Site 463 rocks (Fig. 1), relative to rocks stratigraphically above and below. Ratios of $Fe_{HR}/Fe_{Tot}$ >0.38 imply sediment deposition beneath anoxic waters if ratios of $Fe_{Tot}/Al$ are also >0.5 and $C_{org}$ contents are >0.5 wt% [29, 31]. $Fe_{HR}/Fe_{Tot}$ values recorded in the Cismon core during OAE1a are consistently above 0.38 and indeed have $Fe_{Tot}/Al$ >0.5 along with $C_{org}$ >0.5 wt%, diagnostic of deposition below an anoxic water column (Fig. 2). $Fe_{HR}/Fe_{Tot}$ ratios in rocks that bound OAE1a have $Fe_{HR}/Fe_{Tot}$ <0.38) (Fig. 2). $Fe_{HR}/Fe_{Tot}$ ratios in rocks deposited at DSDP Site 463 also capture intervals with values >0.38 and Fe/Al >0.5, similarly implying deposition under anoxic conditions. Some $Fe_{HR}/Fe_{Tot}$ values in sediments deposited during OAE1a at site 463, however, are below the threshold (>0.38) used to diagnose anoxic ocean conditions and are thus ambiguous to depositional redox state based on Fe-speciation alone. We note however, that Fe-speciation analyses cannot diagnose sediment deposition under oxic conditions. This is because of mass balance–under the current Fe-speciation framework, enrichment of $Fe_{HR}$ at one depositional location by necessity requires its depletion in another. Ratios below 0.38 can thus also result from deposition beneath an anoxic water column and instead likely signify a remobilization of $Fe_{HR}$ from such sites (Fig. 2). In strong contrast, continental margin sediments, like those deposited at the Cismon site, likely served as the main oceanic sinks for remobilized $Fe_{HR}$.

$Fe_{Pyr}/Fe_{HR}$ ratios are a direct measure of the degree of pyritization of the highly reactive $Fe_{HR}$ pool and ratios >0.7 signal deposition under a euxinic water column [27, 28, 32]. Values <0.7 indicate non-pyritized $Fe_{HR}$ and, by definition, reveal insufficient sulphide supply to pyritize the available $Fe_{HR}$ thus precluding accumulation of free sulphide and the development of euxinia. Values <0.7 in sediments deposited under anoxic conditions ($Fe_{HR}/Fe_{Tot}$ >0.38), signal sulphate depletion and a ferruginous water column. All rocks deposited at the Cismon and DSDP 463 sites during the OAE1a interval have $Fe_{Pyr}/Fe_{HR}$ <<0.7 indicating deposition under strictly non-euxinic, ferruginous conditions (Fig. 2).

As an additional test for depositional redox states we examined the distribution of redox sensitive trace elements (RSTE) that can become enriched under anoxic conditions [33, 34]. Sediments from both the Cismon and DSDP 463 sites are highly enriched in some RSTE throughout the OAE1a interval relative to the post Archean average shale (PAAS) [35]. For example, rhenium (Re), an element that is enriched under both ferruginous, and to a lesser degree euxinic conditions, is highly enriched in OAE1a sediments, confirming deposition under anoxic conditions at both sites (Fig. 2a, b). Deposition under euxinic conditions is often accompanied by strong molybdenum (Mo) enrichment and euxinic conditions can be conditionally inferred when sedimentary Mo concentrations are greater than 25 µg $g^{-1}$ [27]. Compilation of Mo concentrations in sediments deposited across OAE1a [36, 37] shows that only 2 out of 162 samples analysed have Mo concentrations greater than the 25 µg $g^{-1}$ threshold (Fig. S8). This lack of Mo enrichment, in light of Re enrichment, supports the Fe-speciation data, which together show deposition under ferruginous rather than euxinic conditions. Concentrations of Mo greater than 25 µg $g^{-1}$ can be achieved through a variety of processes [38], and in isolation, the two samples with greater than 25 µg $g^{-1}$ need not have been deposited under euxinic conditions. Instead, these rare Mo enrichments likely reflect Fe-oxide and OM-Mo shuttling [39]. The general pattern of strong RSTE enrichments (Cr, V, U, Re) with lack of corresponding Mo enrichment in the OAE1a sediments, strongly contrasts observations from modern euxinic sediments [33]. This can be seen when enrichment factors of these RSTE are normalized to the ratio of the Mo enrichment factor in the OAE1a sediments to the enrichment factors of Mo in example modern euxinic basins (Fig. 2c, d). Most strikingly, Cr and Re are on average 350% and 2500% more enriched in the Cismon sediments than in modern euxinic sediments, relative to Mo, respectively (Fig. 2c, d). Based on the contrasting mechanisms that lead to differential RSTE enrichments, our observations are best explained by deposition of OAE1a sediments under strictly ferruginous and non-euxinic conditions.

Geochemical and petrographic information effectively rule out sample storage artefacts, like oxidation of pyrite, and confirm that the conclusion for deposition of OAE1a sediments under ferruginous conditions is robust. Prior work suggests that sedimentary rocks can be subject to sample storage artefacts that develop as a result of exposure to oxygen in the atmosphere and subsequent oxidation of sedimentary pyrite [40, 41]. We consequently took care to work with well-preserved rocks, but nevertheless also evaluated the extent to which post depositional oxidation of $Fe_{Pyr}$ in our samples could have led to false diagnosis of either anoxic or ferruginous conditions (see Supplementary Information section 4). Oxidation converts pyrite and siderite to Fe-(oxyhydr)oxides and thus causes redistribution of Fe from $Fe_{Pyr}$ and $Fe_{Carb}$ to $Fe_{Ox}$. Since these three pools are summed in the $Fe_{HR}$ pool, oxidation would not have impacted $Fe_{HR}/Fe_{Tot}$ or Fe/Al ratios, and thus could not have led to false diagnosis of anoxia based on Fe speciation. Qualitatively, the preservation of both pristine framboidal pyrites (Fig. S2) and abundant $Fe_{Carb}$ (Table S4, S5) is inconsistent with pervasive post depositional sample oxidation. Furthermore, we identify ferruginous conditions on the basis of $Fe_{Pyr}/Fe_{HR} < 0.7$, and since pyrite oxidation would decrease this ratio it could lead to false diagnosis. We therefore tested the extent to which oxidation might have altered $Fe_{Pyr}/Fe_{HR}$ by summing $Fe_{Ox}$, the product of oxidation, and $Fe_{Pyr}$ to come up with a maximum possible pre-oxidation ratio, $Fe'_{Pyr}/Fe_{HR}$. $Fe'_{Pyr}/Fe_{HR}$ ratios in both the Cismon and DSDP site 463 sediments are mostly below the conservative <0.7 threshold for the delineation of ferruginous conditions (Fig. 2). This implies our conclusions are robust even in the unlikely scenario where the entire $Fe_{Ox}$ pool represents the product of pyrite oxidation. Likewise, if total S (pyrite S and any S pool resulting from oxidation) is used as a proxy for pre-oxidation pyrite ($Fe''_{Pyr}$), $Fe''_{Pyr}/Fe_{HR}$ also remain mostly below the 0.7 threshold (Fig. S2). We also note, that our RSTE data would be unaffected by sample oxidation. Collectively, therefore, our Fe speciation and RSTE data unambiguously document deposition of both DSDP and Cismon sediments under ferruginous conditions.

## Aptian seawater sulphate concentrations

To constrain Aptian seawater sulphate concentrations, we constructed a 1D water-column reactive transport model (see Supplementary Information) to simulate complete sulphate drawdown through microbial sulphate reduction that would permit the development of ferruginous conditions in a stratified Cretaceous ocean. Pyrite burial fluxes calculated by combining sedimentation rates [26] with sediment pyrite concentrations tether our 1D water column model outputs to the geologic record and place upper limits on the flux of sulphate that can be converted to pyrite through microbial sulphate reduction and reaction of the sulphide produced with $Fe_{HR}$, either directly in the water column or in bottom sediments (see Supplementary Information section 6). With microbial sulphate reduction rates parameterized based on modern marine ecosystems and analogies to low-sulphate ferruginous environments [42, 43] our water column modelling yields an average estimate for seawater sulphate of 5-10 μM, but not more than 70 μM (Fig. 3). Similar results are obtained modelling sulphate reduction rates in underlying sediments (Table S8). We note that the low sulphate reduction rates in our models are also consistent with the large S-isotope fractionations observed in Cismon pyrites and pyrites deposited elsewhere during OAE1a [15], given that large S-isotope fractionations tend to develop at low sulphate reduction rates [44]. The large S-isotope fractionations recorded in the Cismon pyrites, however, may also require a contribution from S disproportionation ($\delta^{34}S_{pyrite} \approx -47‰$ [13], Fig. S4) which is known to be active in modern Fe-rich sediments [45]. Imposing higher sulphate concentrations in our models with realistic rates of sulphate reduction, sedimentation rates, and transport across oceanic pycnoclines or the sediment-water interface, yield pyrite burial fluxes much higher than those recorded in Cismon rocks. Alternatively, these lead to residual sulphate in deep waters and are thus incompatible with the Fe speciation data and ferruginous depositional conditions (Fig 3). Our results thus constrain seawater sulphate concentrations during OAE1a, to more than a hundred times lower than the modern.

Our observation of ferruginous conditions during OAE1a require a decline of the seawater sulphate pool from low mM to µM concentrations in a time frame of less than 100 kyr, commensurate with the initiation of OAE1a, as delineated by the carbon isotope record. Previous studies suggest that seawater sulphate concentrations were drawn down to as low as 1 mM over millions of years preceding OAE1a as the result of evaporite deposition associated with the opening of the South Atlantic [17]. Evaporite mineral deposition effectively draws sulphate down from modern day concentrations of 28 mM to 1 mM, but when sulphate concentrations drop below 1 mM, seawater saturation with respect to sulphate-minerals (gypsum) during evaporation requires unrealistically high $Ca^{2+}$ concentrations that are inconsistent with reconstructions for Aptian seawater chemistry [12, 46] (see Supplementary Information). Our observation of ferruginous conditions and sub-mM seawater sulphate concentrations thus effectively rules out contemporaneous deposition of black shale and gypsum in evaporites during the OAE1a interval itself. This instead implies that evaporite deposition took place before OAE1a, in the Late Barremian to early Aptian as previously considered [21]. Seawater sulphate drawdown to µM concentrations therefore requires a second phase of sulphate sequestration and alternative burial mechanisms. Another important sink for seawater sulphate is microbial sulphate reduction and pyrite deposition and burial. Expansion of this sink during OAE1a provides a plausible mechanism to lower seawater sulphate to µM concentrations and drive development of ferruginous conditions, which we explore below.

Enhanced pyrite burial associated with the expansion of ocean anoxia helps balance strong hydrothermal and weathering inputs of S to the oceans during OAE1a. Coupled models of strontium and sulphur isotopes provide compelling evidence for enhanced hydrothermalism and continental weathering at this time [14, 15]. The development of ferruginous conditions as well as S budgets and S isotope mass balances (see Supplementary Information), however, require additional sinks for marine sulphate that balance these enhanced S inputs. Sulphur mass balance modelling reveals that an increase in global pyrite deposition rates from 0.66 to a maximum of 2.9 Tmol $yr^{-1}$ (Fig 4a), offsets some of the enhanced S inputs while remaining consistent with the isotope record (Fig. 4b). We note that pyrite deposition rates are higher under anoxic water columns [47] and thus the increase in pyrite burial could be achieved by expanding the global extent of water column anoxia. For example, if water column anoxia expanded from 0.1%, its extent in the modern ocean [48], to between 2 and 10%, the increase from 0.66 to 2.9 Tmol $yr^{-1}$ could be achieved with area specific pyrite deposition rates between 0.08 and 0.4 mol S $m^{-2}$ $yr^{-1}$ in regions of ocean anoxia, which is similar to rates of pyrite burial in sediments underlying modern OMZs [49, 50] (Fig. 4a and Supplementary Information Fig. S6). This pyrite burial interval would also drive an increase in the $\delta^{34}S$ composition of seawater sulphate due to enhanced burial of isotopically light S in pyrite. Such an increase in seawater sulphate $\delta^{34}S$ appears to be recorded in some carbonate associated sulphate (CAS), providing geological evidence for such pyrite burial (Fig 4c) [14, 15]. Mass balance using this same S isotope data constrains maximum pyrite depositional rates to not much more than 2.9 Tmol $yr^{-1}$, yet given the strong input fluxes from hydrothermalism and weathering another S sink is needed to draw seawater sulphate concentrations down to levels that support ferruginous conditions.

Biomass associated organic S is an additional, yet often overlooked, sulphur sink that when combined with pyrite burial, is sufficiently large to draw seawater sulphate down to μM concentrations. S-isotope mass balance requires that this additional sink carries near seawater $\delta^{34}S$ values. Sinks such as biomass derived organic S, CAS, or barite associated with organic matter, are all known to operate in low sulphate modern and ancient environments [51, 52]. While biomass associated organic S has been shown to be a major pathway for S burial in lacustrine environments [53, 54], it is often neglected in the marine S cycle. Marine organisms are characterized by C:S molar ratios of 50:1 [55, 56, 57], and thus the burial flux of organic S is likely on the order of 5 wt% that of organic C. Note that this biomass associated organic S is distinct from S added to OM during diagenesis (i.e., through sulphurization reactions [58]). Given the total S and organic matter contents of the Cismon sediments deposited during OAE1a [59], and assuming all non-pyrite S is buried as biomass associated organic S, we calculate an average OM C:S molar ratio of ~45, revealing that OM buried during OAE1a has a similar C:S composition to that of modern biomass [57]. This supports the idea that during intervals of increased OM burial, biomass associated organic S is an important sink from the ocean. Marine organisms, furthermore, assimilate S with a $\delta^{34}S$ composition nearly identical to seawater [56, 60, 61]. Given pre-OAE1a primary production similar to modern (48 Gt C $yr^{-1}$) [48] and OM that is ~5 wt% S, the dramatic (up to a 35-fold [59]) increase in OM burial during OAE1a would be, together with pyrite burial, more than sufficient (up to 7.5 Tmol $yr^{-1}$) to remove most of the S entering the ocean at this time (5.3 Tmol $yr^{-1}$). Development of ferruginous conditions can thus be attributed to widespread anoxia and ensuing pelagic sulphate reduction and enhanced burial of biomass associated organic S against the backdrop of low Cretaceous seawater sulphate concentrations as well as strong hydrothermalism and weathering. Following OAE1a, the seawater sulphate pool can rebound to mM sulphate concentrations in less than 2 Myr (Fig 4b), allowing for evaporite deposition as early as ~122 Ma, a timing also consistent with known post OAE1a evaporite stratigraphies [20].

## Implications

At 28 mM, seawater sulphate is an oxidant pool twice the size of modern atmospheric $O_2$. A decline to low μM seawater sulphate concentrations thus indicates a reorganization of global oxidant pools during OAE1a with implications for marine ecology, biogeochemical cycling, and climate. Water column anoxia, for example, may have extended at least transiently into the photic zone during OAE1a with potential to influence photosynthetic ecology. Biomarkers indicative of green S bacteria have indeed been recovered in sediments deposited during

OAE1a [62, 63]. While green S bacteria are best known as sulphide oxidizing phototrophs [64], they are also known to grow on ferrous Fe (photoferrotrophy) and were likely key primary producers in the ferruginous oceans of the Precambrian [65]. Preservation of biomarkers from green S bacteria in Aptian ferruginous sediments may thus signal the return of photoferrotrophy to the Phanerozoic oceans. At the same time, low-sulphate, ferruginous ocean conditions would have both channelled organic matter degradation from sulphate reduction to methanogenesis and precluded the consumption of this methane through anaerobic oxidation with sulphate. Earth system modelling indeed shows that seawater sulphate concentrations below 1 mM promote massive marine methane fluxes to the atmosphere with attendant greenhouse warming [24].

Development of ferruginous conditions during OAE1a thus reveals large-scale dynamics in Earth's biogeochemical cycles over intervals of less than a hundred thousand years (Fig. 4). The development of ferruginous ocean conditions during multiple OAEs [8, 11] may thus signify a general instability in Earth surface redox budgets and the recurrent reorganization of major oxidant pools at Earth's surface, like seawater sulphate, during the Phanerozoic Eon. The mechanisms driving this reorganization remain uncertain, but could be addressed through better constraints on global S budgets and the drivers of ocean de-oxygenation, as well as the development of Earth system models that resolve such large-scale biogeochemical dynamics over relatively short time scales.

## Figure Captions

Figure 1. Fe-speciation and carbon isotope records for Cismon and DSDP Site 463. Integrated stratigraphy of the Cismon and DSDP Site 463 after [25, 66]. The grey shaded region (OAE1a) represents ~1.1 Mya [26], C-isotope stages C2–C7 [14, 26, 67]. Panels (a-e) are Cismon data and panels (f-j) are DSDP Site 463 data (**a**) Cismon carbon isotope data from [66]. Rhenium concentration data from [59]. (**b**) Carbonate C after [68], and organic matter C data after [59]. (**c**) $Fe_{Pyritizable}$; sum of all pyritizable $Fe_{HR}$ pools ($Fe_{Carb}$, $Fe_{OM}$, $Fe_{Ox}$) (**d**) $Fe_{Sil}$; silicate Fe (**e**) $Fe_{Pyr}$; pyrite Fe. Green diamonds represent pyrite concentration data from [13]. (**f**) DSDP Site 463 carbon isotope data from [59]. Rhenium concentration data from [59]. (**g**) Carbonate C data from [66], organic C data from [63, 66]. (**h**) $Fe_{Pyritizable}$; sum of all pyritizable $Fe_{HR}$ pools ($Fe_{Carb}$, $Fe_{OM}$, $Fe_{Ox}$) (**i**) $Fe_{Sil}$; silicate Fe. (**j**) $Fe_{Pyr}$; pyrite Fe. The start of the nannoconid decline and beginning of the nannoconid crisis are marked with dashed lines [25].

Figure 2. (**a**) Fe-speciation and Fe/Al records of the Cismon and DSDP Site 463 (**b**). The vertical and horizontal dotted lines refer to the oxic-anoxic threshold ($Fe_{HR}/Fe_{Tot} = 0.38$) and a conservative ferruginous-euxinic threshold ($Fe_{Pyr}/Fe_{HR} = 0.70$) respectively. The open circles represent $Fe'_{Pyr}/Fe_{HR}$, the maximum possible amount of pyrite present in the samples assuming the very unlikely scenario where the entire $Fe_{Ox}$ pool is a result of pyrite oxidation. The solid vertical line in the top panels refers to the Fe/Al ratio of 0.5. The solid vertical line in the bottom panels refers to the average rhenium concentration of the PAAS, with the purple shading representing a 2 sigma uncertainty on this value (0.4 pbb, [69]). Litho-, bio- and magneto-stratigraphy is the same as for Figure 1. OAE1a redox sensitive trace element (RSTE) enrichment factors for the Cismon core (**c**) and DSDP site 463 (**d**) compared to modern euxinic sediments. Displayed are enrichment factors of RSTE normalized to the ratio of the Mo enrichment factor in the OAE1a sediments to the enrichment factors of Mo in example modern euxinic basins, Cariaco Basin and Saanich Inlet sediments. We find that the RSTE enrichment factors of Cr and Re, metals that do not require free sulphide to be buried under anoxic conditions, are dramatically enriched in both the Cismon and DSDP 463 sediments, relative to modern euxinic basins.

Figure 3. Models of marine S cycling during OAE1a. (**a**) Modelled rates of microbial sulphate reduction in a stratified ocean water column with different surface seawater sulphate concentrations. The upper 100 m represents the surface mixed layer, which we assume is well oxygenated. (**b**) Resulting sulphate concentration profiles. (**c**) Water column depth integrated sulphate reduction rates (pyrite burial). The parameter space represents modelled depth integrated sulphate reduction rates consistent with complete water column sulphate drawdown, as a function of initial seawater sulphate concentration and the maximum rate of sulphate reduction ($V_{max}$). To conservatively allow for uncertainties in the sedimentation rate at the Cismon site, we scaled up the average pyrite depositional flux determined for the Cismon sediments by two factors; 7.8 ($C_{Pyr}^{7.8}$) to allow for the possibility of higher sedimentation rates like those observed in modern environments like the Peru Margin and Black Sea, and 25 ($C_{Pyr}^{25}$), to allow for even higher sedimentation rates like those observed in the modern Cariaco Basin. Such higher sedimentation rates would lead to higher pyrite burial fluxes in the Cismon and DSDP site 463 sediments, and would support higher upper estimates on the flux of

sulphate that can be converted to pyrite through microbial sulphate reduction. The pink box outlines the solution space corresponding to the average pyrite depositional flux observed in the Cismon sediments (350 $\mu$mol $m^{-2}$ $yr^{-1}$), including the upper estimate produced by the scaling factor ($C_{Pyr}^{7.8}$), whereas the green box solution space outlines the range of pyrite depositional fluxes observed at the Cismon site scaled for even higher sedimentation rates ($C_{Pyr}^{25}$). We note that imposing higher rates of water column sulphate reduction in our model leads to pyrite deposition rates much higher than those recorded in the Cismon and DSDP site 463 sediments during OAE1a.

Figure 4. Evolution of the Cretaceous seawater sulphate reservoir. The coloured bars represent the conceptual model and proposed timing of early Cretaceous events associated with the development of OAE1a [13, 20, 21, 59]. (**a**) Modelled S input and burial fluxes. The blue line represents hydrothermal and weathering S input after [14, 15]. The black line is our modelled pyrite burial flux. The pink line represents the burial of S in evaporites and the green line represents a non-fractionated sink of S needed to account for total S burial during OAE1a. (**b**) The blue line is our model result for the evolution of seawater sulphate concentrations. The green shading represents the relative timing of OAE1a. (**c**) Isotopic composition of Aptian seawater sulphate. The blue line represents our model results for the evolution of $\delta^{34}S_{sulphate}$. The grey data points represent $\delta^{34}S_{sulphate}$ data from [14]; squares, [15]; diamonds, [70]; crosses and [13]; triangles. The diamond distribution plot at the right is a compilation of this sedimentary $\delta^{34}S_{Sulphate}$ data with the grey shading delineating the 5th and 95th percentiles, encompassing 90% of the early Aptian $\delta^{34}S_{Sulphate}$ data.

## Acknowledgements

This work was funded through NSERC Discovery Grants to Sean A. Crowe (0487) and Roger Francois, the Canadian Foundation for Innovation, the Canada Research Chairs Program, and a UBC 4-Year Fellowship. We thank the Integrated Ocean Drilling Program (IODP) for providing the DSDP Site 463 samples. We thank John Greenough for help with the milling of rock samples. We also acknowledge Steve Calvert for participating in helpful discussions on rhenium geochemistry.

## Data availability statement

The datasets and models generated during and/or analysed during the current study are available from the corresponding author on reasonable request.

1. Kump LR, Brantley SL, Arthur MA. Chemical, weathering, atmospheric CO2, and climate. *Annual Review of Earth and Planetary Sciences* 2000, **28:** 611-667.

2. Stolper DA, Keller CB. A record of deep-ocean dissolved O2 from the oxidation state of iron in submarine basalts. *Nature* 2018, **553**(7688)**:** 323-327.

3. Planavsky NJ, Reinhard CT, Wang X, Thomson D, McGoldrick P, Rainbird RH, *et al.* Low Mid-Proterozoic atmospheric oxygen levels and the delayed rise of animals. *Science* 2014, **346**(6209)**:** 635-638.

4. Poulton SW, Canfield DE. Ferruginous Conditions: A Dominant Feature of the Ocean through Earth's History. *Elements* 2011, **7**(2)**:** 107-112.

5. Berner RA, Canfield DE. A new model for atmospheric oxygen over Phanerozoic time. *American Journal of Science* 1989, **289**(4)**:** 333-361.

6. Bergman NM, Lenton TM, Watson AJ. COPSE: A new model of biogeochemical cycling over Phanerozoic time. *American Journal of Science* 2004, **304**(5)**:** 397-437.

7. Jenkyns HC. Geochemistry of oceanic anoxic events. *Geochemistry Geophysics Geosystems* 2010, **11:** 30.

8. Poulton SW, Henkel S, Marz C, Urquhart H, Flogel S, Kasten S*, et al.* A continental-weathering control on orbitally driven redox-nutrient cycling during Cretaceous Oceanic Anoxic Event 2. *Geology* 2015, **43**(11)**:** 963-966.

9. Kuypers MMM, Pancost RD, Nijenhuis IA, Damste JSS. Enhanced productivity led to increased organic carbon burial in the euxinic North Atlantic basin during the late Cenomanian oceanic anoxic event. *Paleoceanography* 2002, **17**(4).

10. Marz C, Poulton SW, Beckmann B, Kuster K, Wagner T, Kasten S. Redox sensitivity of P cycling during marine black shale formation: Dynamics of sulfidic and anoxic, non-sulfidic bottom waters. *Geochimica Et Cosmochimica Acta* 2008, **72**(15)**:** 3703-3717.

11. Clarkson MO, Wood RA, Poulton SW, Richoz S, Newton RJ, Kasemann SA*, et al.* Dynamic anoxic ferruginous conditions during the end-Permian mass extinction and recovery. *Nature Communications* 2016, **7**.

12. Timofeeff MN, Lowenstein TK, da Silva MA, Harris NB. Secular variation in the major-ion chemistry of seawater: Evidence from fluid inclusions in Cretaceous halites. *Geochimica Et Cosmochimica Acta* 2006, **70**(8).

13. Gomes ML, Hurtgen MT, Sageman BB. Biogeochemical sulfur cycling during Cretaceous oceanic anoxic events: A comparison of OAE1a and OAE2. *Paleoceanography* 2016, **31**(2)**:** 233-251.

14. Mills JV, Gomes ML, Kristall B, Sageman BB, Jacobson AD, Hurtgen MT. Massive volcanism, evaporite deposition, and the chemical evolution of the Early Cretaceous ocean. *Geology* 2017, **45**(5)**:** 475-478.

15. Kristall B, Jacobson AD, Sageman BB, Hurtgen MT. Coupled strontium-sulfur cycle modeling and the Early Cretaceous sulfur isotope record. *Palaeogeography Palaeoclimatology Palaeoecology* 2018, **496:** 305-322.

16. Lowenstein TK, Hardie LA, Timofeeff MN, Demicco RV. Secular variation in seawater chemistry and the origin of calcium chloride basinal brines. *Geology* 2003, **31**(10)**:** 857-860.

17. Wortmann UG, Chernyavsky BM. Effect of evaporite deposition on Early Cretaceous carbon and sulphur cycling. *Nature* 2007, **446**(7136)**:** 654-656.

18. Davison I. Geology and tectonics of the South Atlantic Brazilian salt basins. *Geological Society, London, Special Publications* 2007, **272**(1)**:** 345-359.

19. Bate RH. Non-marine ostracod assemblages of the Pre-Salt rift basins of West Africa and their role in sequence stratigraphy. *Geological Society, London, Special Publications* 1999, **153**(1)**:** 283-292.

20. Chaboureau AC, Guillocheau F, Robin C, Rohais S, Moulin M, Aslanian D. Paleogeographic evolution of the central segment of the South Atlantic during Early Cretaceous times: Paleotopographic and geodynamic implications. *Tectonophysics* 2013, **604:** 191-223.

21. Tedeschi LR, Jenkyns HC, Robinson SA, Sanjines AES, Viviers MC, Quintaes C*, et al.* New age constraints on Aptian evaporites and carbonates from the South Atlantic: Implications for Oceanic Anoxic Event 1a. *Geology* 2017, **45**(6)**:** 543-546.

22. Knittel K, Boetius A. Anaerobic Oxidation of Methane: Progress with an Unknown Process. *Annual Review of Microbiology* 2009, **63:** 311-334.

23. Reeburgh WS. Oceanic methane biogeochemistry. *Chemical Reviews* 2007, **107**(2)**:** 486-513.

24. Olson SL, Reinhard CT, Lyons TW. Limited role for methane in the mid-Proterozoic greenhouse. *Proceedings of the National Academy of Sciences of the United States of America* 2016, **113**(41)**:** 11447-11452.

25. Erba E, Bottini C, Weissert HJ, Keller CE. Calcareous Nannoplankton Response to Surface-Water Acidification Around Oceanic Anoxic Event 1a. *Science* 2010, **329**(5990)**:** 428-432.

26. Malinverno A, Erba E, Herbert TD. Orbital tuning as an inverse problem: Chronology of the early Aptian oceanic anoxic event 1a (Selli Level) in the Cismon APTICORE. *Paleoceanography* 2010, **25**.

27. Lyons TW, Severmann S. A critical look at iron paleoredox proxies: New insights from modern euxinic marine basins. *Geochimica Et Cosmochimica Acta* 2006, **70**(23)**:** 5698-5722.

28. Canfield DE, Raiswell R, Bottrell S. The reactivity of sedimentary iron minerals toward sulfide. *American Journal of Science* 1992, **292**(9)**:** 659-683.

29. Poulton SW, Canfield DE. Development of a sequential extraction procedure for iron: implications for iron partitioning in continentally derived particulates. *Chemical Geology* 2005, **214**(3-4)**:** 209-221.

30. Canfield DE, Thamdrup B, Hansen JW. The anaerobic degradation of organic matter in Danish coastal sediments: iron reduction, manganese reduction, and sulfate reduction. *Geochimica Et Cosmochimica Acta* 1993, **57**(16)**:** 3867-3883.

31. Clarkson MO, Poulton SW, Guilbaud R, Wood RA. Assessing the utility of Fe/Al and Fe-speciation to record water column redox conditions in carbonate-rich sediments. *Chemical Geology* 2014, **382:** 111-122.

32. Poulton SW, Fralick PW, Canfield DE. The transition to a sulphidic ocean similar to 1.84 billion years ago. *Nature* 2004, **431**(7005)**:** 173-177.

33. Calvert SE, Pedersen TF. Geochemistry of recent oxic and anoxic marine sediments: implications for the geological record. *Mar Geol* 1993, **113**(1-2)**:** 67-88.

34. Tribovillard N, Algeo TJ, Lyons T, Riboulleau A. Trace metals as paleoredox and paleoproductivity proxies: An update. *Chemical Geology* 2006, **232**(1-2)**:** 12-32.

35. McLennan SM. Relationships between the trace element composition of sedimentary rocks and upper continental crust. *Geochemistry Geophysics Geosystems* 2001, **2:** art. no.-2000GC000109.

36. Westermann S, Stein M, Matera V, Fiet N, Fleitmann D, Adatte T, *et al.* Rapid changes in the redox conditions of the western Tethys Ocean during the early

Aptian oceanic anoxic event. *Geochimica Et Cosmochimica Acta* 2013, **121:** 467-486.

37. Follmi KB. Early Cretaceous life, climate and anoxia. *Cretaceous Research* 2012, **35:** 230-257.

38. Hardisty DS, Lyons TW, Riedinger N, Isson TT, Owens JD, Aller RC*, et al.* An evaluation of sedimentary molybdenum and iron as proxies for pore fluid paleoredox conditions. *American Journal of Science* 2018, **318**(5)**:** 527-556.

39. Bertine KK, Turekian KK. Molybdenum in marine deposits. *Geochimica et Cosmochimica Acta* 1973, **37**(6)**:** 1415-1434.

40. Slotznick SP, Eiler JM, Fischer WW. The effects of metamorphism on iron mineralogy and the iron speciation redox proxy. *Geochimica Et Cosmochimica Acta* 2018, **224:** 96-115.

41. Kraal P, Slomp CP, Forster A, Kuypers MMM, Sluijs A. Pyrite oxidation during sample storage determines phosphorus fractionation in carbonate-poor anoxic sediments. *Geochimica Et Cosmochimica Acta* 2009, **73**(11)**:** 3277-3290.

42. Crowe SA, Maresca JA, Jones C, Sturm A, Henny C, Fowle DA*, et al.* Deep-water anoxygenic photosythesis in a ferruginous chemocline. *Geobiology* 2014, **12**(4)**:** 322-339.

43. Canfield DE, Stewart FJ, Thamdrup B, De Brabandere L, Dalsgaard T, Delong EF*, et al.* A Cryptic Sulfur Cycle in Oxygen-Minimum-Zone Waters off the Chilean Coast. *Science* 2010, **330**(6009)**:** 1375-1378.

44. Habicht KS, Canfield DE. Sulfur isotope fractionation during bacterial sulfate reduction in organic-rich sediments. *Geochimica Et Cosmochimica Acta* 1997, **61**(24)**:** 5351-5361.

45. Kunzmann M, Bui TH, Crockford PW, Halverson GP, Scott C, Lyons TW*, et al.* Bacterial sulfur disproportionation constrains timing of Neoproterozoic oxygenation. *Geology* 2017, **45**(3)**:** 207-210.

46. Blattler CL, Jenkyns HC, Reynard LM, Henderson GM. Significant increases in global weathering during Oceanic Anoxic Events 1a and 2 indicated by calcium isotopes. *Earth and Planetary Science Letters* 2011, **309**(1-2)**:** 77-88.

47. Calvert SE, Karlin RE. Relationships between sulphur, organic carbon, and iron in the modern sediments of the Black Sea. *Geochimica Et Cosmochimica Acta* 1991, **55**(9)**:** 2483-2490.

48. Martin JH, Knauer GA, Karl DM, Broenkow WW. VERTEX: carbon cycling in the northeast Pacific. *Deep Sea Research Part A Oceanographic Research Papers* 1987, **34**(2)**:** 267-285.

49. Böning P. Trace element signatures of Peruvian and Chilean upwelling sediments. Universität Oldenburg, 2005.

50. Scholz F, Severmann S, McManus J, Noffke A, Lomnitz U, Hensen C. On the isotope composition of reactive iron in marine sediments: Redox shuttle versus early diagenesis. *Chemical Geology* 2014, **389:** 48-59.

51. Horner TJ, Pryer HV, Nielsen SG, Crockford PW, Gauglitz JM, Wing BA*, et al.* Pelagic barite precipitation at micromolar ambient sulfate. *Nature Communications* 2017, **8**.

52. Paris G, Adkins JF, Sessions AL, Webb SM, Fischer WW. Neoarchean carbonate-associated sulfate records positive Delta S-33 anomalies. *Science* 2014, **346**(6210)**:** 739-741.

53. Mitchell MJ, Landers DH, Brodowski DF, Lawrence GB, David MB. Organic and inorganic sulfur constituents of the sediments in three New York lakes: Effect of site, sediment depth and season. *Water Air and Soil Pollution* 1984, **21**(1-4)**:** 231-245.

54. Urban NR. Retention of sulfur in lake sediments. *Environmental Chemistry of Lakes and Reservoirs* 1994, **237:** 323-369.

55. Fagerbakke KM, Heldal M, Norland S. Content of carbon, nitrogen, oxygen, sulfur and phosphorus in native aquatic and cultured bacteria. *Aquatic Microbial Ecology* 1996, **10**(1)**:** 15-27.

56. Kaplan IR, Emery KO, Rittenberg SC. The distribution and isotopic abundance of sulphur in recent marine sediments off southern California. *Geochimica Et Cosmochimica Acta* 1963, **27**(APR)**:** 297-&.

57. Chen CTA, Lin CM, Huang BT, Chang LF. Stoichiometry of carbon, hydrogen, nitrogen, sulfur and oxygen in the particulate matter of the western North Pacific marginal seas. *Marine Chemistry* 1996, **54**(1-2)**:** 179-190.

58. Raven MR, Fike DA, Gomes ML, Webb SM, Bradley AS, McClelland HLO. Organic carbon burial during OAE2 driven by changes in the locus of organic matter sulfurization. *Nature Communications* 2018, **9**.

59. Bottini C, Cohen AS, Erba E, Jenkyns HC, Coe AL. Osmium-isotope evidence for volcanism, weathering, and ocean mixing during the early Aptian OAE 1a. *Geology* 2012, **40**(7)**:** 583-586.

60. Kaplan IR, Rittenberg SC. Microbiological fractionation of sulphur isotopes. *Journal of General Microbiology* 1964, **34**(2)**:** 195-&.

61. Utne-Palm AC, Salvanes AGV, Currie B, Kaartvedt S, Nilsson GE, Braithwaite VA*, et al.* Trophic Structure and Community Stability in an Overfished Ecosystem. *Science* 2010, **329**(5989)**:** 333-336.

62. Damste JSS, Wakeham SG, Kohnen MEL, Hayes JM, Deleeuw JW. A 6,000–year sedimentary molecular record of chemocline excursions in the Black Sea. *Nature* 1993, **362**(6423)**:** 827-829.

63. van Breugel Y, Schouten S, Tsikos H, Erba E, Price GD, Damste JSS. Synchronous negative carbon isotope shifts in marine and terrestrial biomarkers at the onset of the early Aptian oceanic anoxic event 1a: Evidence for the release of C-13-depleted carbon into the atmosphere. *Paleoceanography* 2007, **22**(1).

64. Canfield DE, Teske A. Late Proterozoic rise in atmospheric oxygen concentration inferred from phylogenetic and sulphur-isotope studies. *Nature* 1996, **382**(6587)**:** 127-132.

65. Crowe SA, Jones C, Katsev S, Magen C, O'Neill AH, Sturm A*, et al.* Photoferrotrophs thrive in an Archean Ocean analogue. *Proceedings of the National Academy of Sciences of the United States of America* 2008, **105**(41)**:** 15938-15943.

66. Bottini C, Erba E, Tiraboschi D, Jenkyns H, Schouten S, Sinninghe Damsté J. Climate variability and ocean fertility during the Aptian Stage. *Climate of the Past* 2015, **11**(3)**:** 383-402.

67. Menegatti AP, Weissert H, Brown RS, Tyson RV, Farrimond P, Strasser A*, et al.* High-resolution delta C-13 stratigraphy through the early Aptian "Livello Selli" of the Alpine Tethys. *Paleoceanography* 1998, **13**(5).

68. Li Y-X, Bralower TJ, Montañez IP, Osleger DA, Arthur MA, Bice DM*, et al.* Toward an orbital chronology for the early Aptian oceanic anoxic event (OAE1a,~ 120 Ma). *Earth and Planetary Science Letters* 2008, **271**(1)**:** 88-100.

69. Li Y, Schoonmaker J. *Chemical composition and mineralogy of marine sediments*, vol. 7. na, 2003.

70. Paytan A, Kastner M, Campbell D, Thiemens MH. Seawater sulfur isotope fluctuations in the cretaceous. *Science* 2004, **304**(5677)**:** 1663-1665.

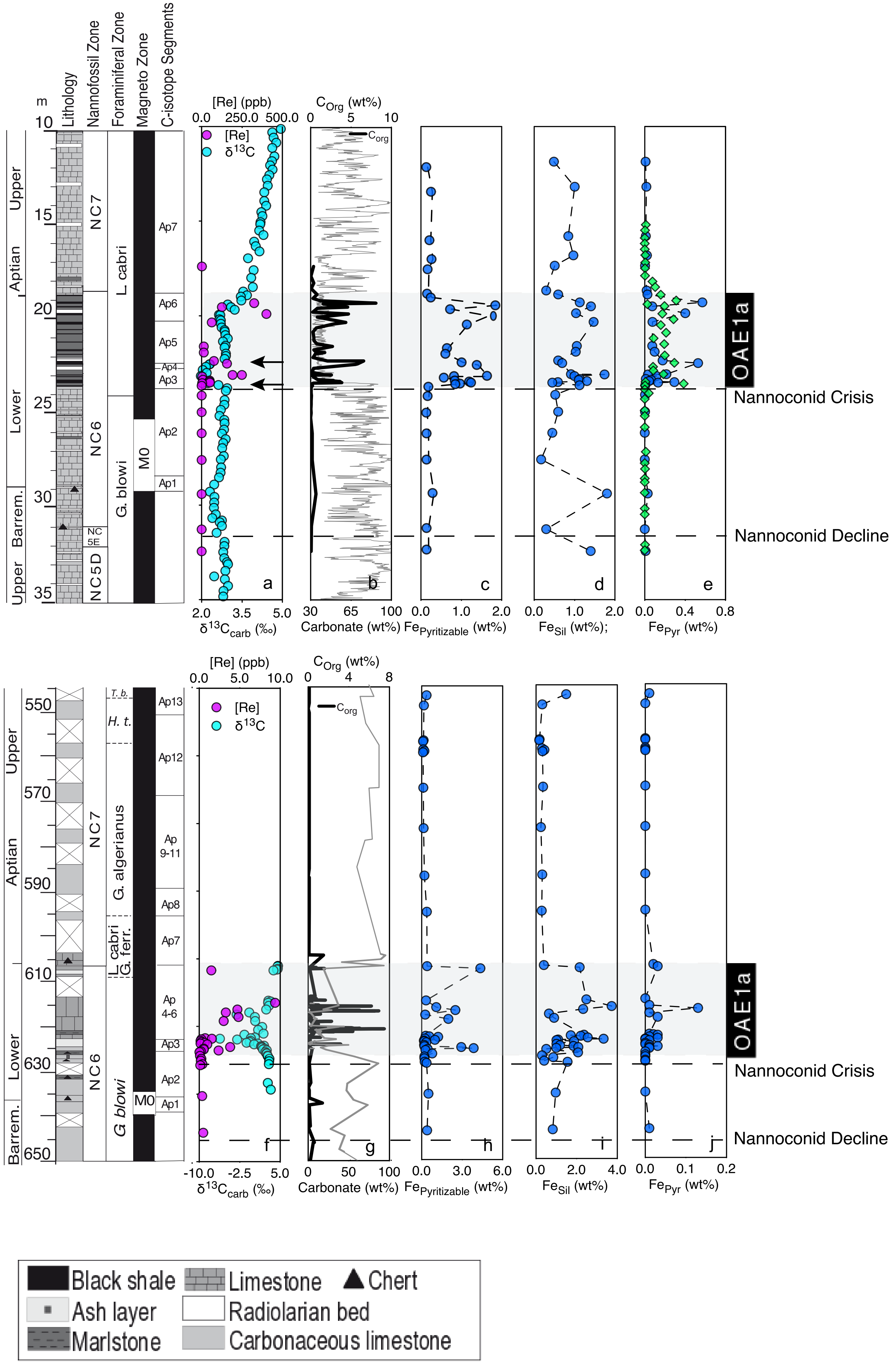
m
Lithology
Nannofossil Zone
Foraminiferal Zone
Magneto Zone
C-isotope Segments
Upper
Aptian
Lower
Barrem.
NC7
NC6
NC 5E
NC5D
L cabri
G. blowi
M0
Ap7
Ap6
Ap5
Ap4
Ap3
Ap2
Ap1
[Re] (ppb)
0.0 250.0 500.0
[Re]
δ13C
$\delta^{13}C_{carb}$ (‰)
$C_{Org}$ (wt%)
$C_{org}$
Carbonate (wt%)
$Fe_{Pyritizable}$ (wt%)
$Fe_{Sil}$ (wt%);
$Fe_{Pyr}$ (wt%)
a
b
c
d
e
OAE1a
Nannoconid Crisis
Nannoconid Decline
T. b.
H. t.
G. algerianus
L cabri G. ferr.
G blowi
Ap13
Ap12
Ap 9-11
Ap8
Ap 4-6
f
g
h
i
j
0.0 5.0 10.0
-10.0 -2.5 5.0
Black shale
Limestone
Chert
Ash layer
Radiolarian bed
Marlstone
Carbonaceous limestone

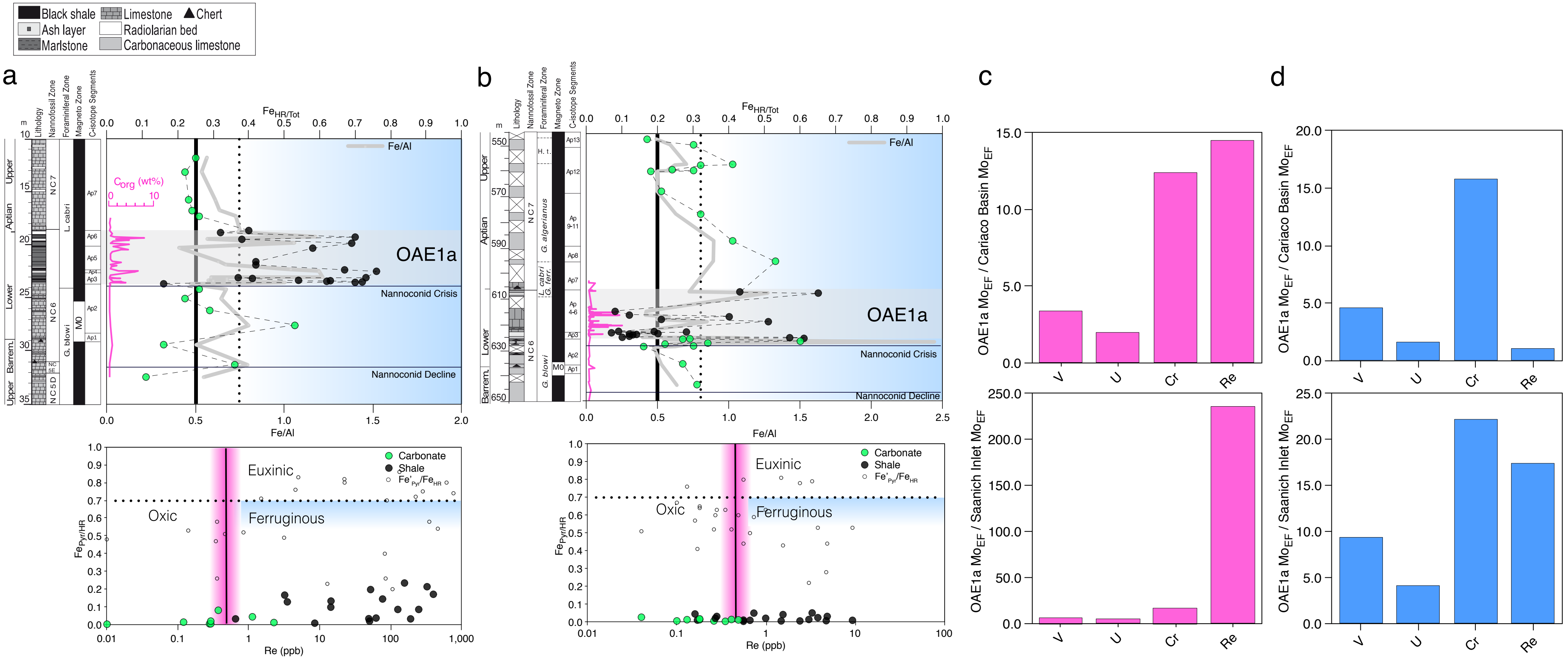

Black shale
Limestone
Chert
Ash layer
Radiolarian bed
Marlstone
Carbonaceous limestone
a
b
c
d
m
Lithology
Nannofossil Zone
Foraminiferal Zone
Magneto Zone
C-isotope Segments
Fe$_{HR/Tot}$
Fe/Al
$C_{org}$ (wt%)
OAE1a
Nannoconid Crisis
Nannoconid Decline
Upper
Aptian
Lower
Barrem.
NC7
NC6
NC5D
NC 5E
L. cabri
G. blowi
G. algerianus
G. ferr.
H. t.
M0
Ap1
Ap2
Ap3
Ap4
Ap5
Ap6
Ap7
Ap 4-6
Ap8
Ap 9-11
Ap12
Ap13
Fe/Al
Re (ppb)
Fe$_{Pyr/HR}$
Euxinic
Oxic
Ferruginous
Carbonate
Shale
Fe'$_{Pyr}$/Fe$_{HR}$
OAE1a Mo$_{EF}$ / Cariaco Basin Mo$_{EF}$
OAE1a Mo$_{EF}$ / Saanich Inlet Mo$_{EF}$
V
U
Cr
Re

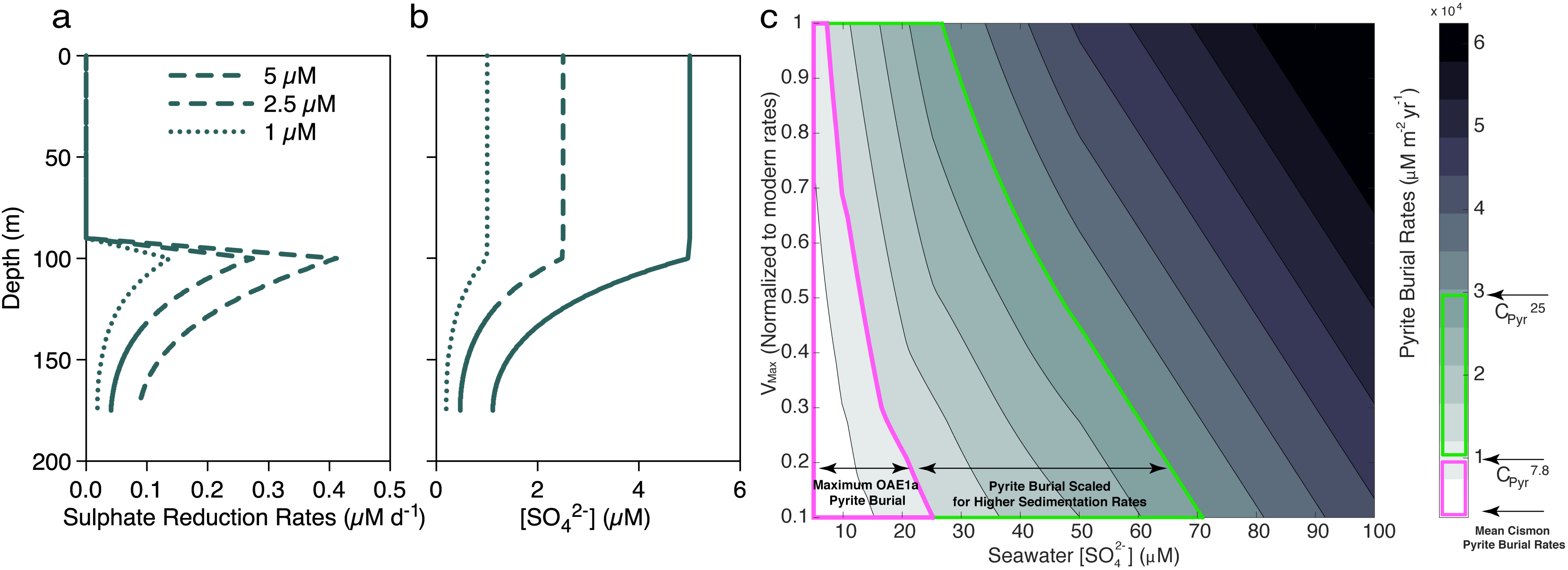
a
b
c
5 μM
2.5 μM
1 μM
Depth (m)
0
50
100
150
200
0.0
0.1
0.2
0.3
0.4
0.5
Sulphate Reduction Rates (μM d^-1)
0
2
4
6
[SO4 2-] (μM)
V_Max (Normalized to modern rates)
1
0.9
0.8
0.7
0.6
0.5
0.4
0.3
0.2
0.1
10
20
30
40
50
60
70
80
90
100
Seawater [SO4 2-] (μM)
Maximum OAE1a
Pyrite Burial
Pyrite Burial Scaled
for Higher Sedimentation Rates
x 10^4
6
5
4
3
2
1
Pyrite Burial Rates (μM m^-2 yr^-1)
C_Pyr 25
C_Pyr 7.8
Mean Cismon
Pyrite Burial Rates

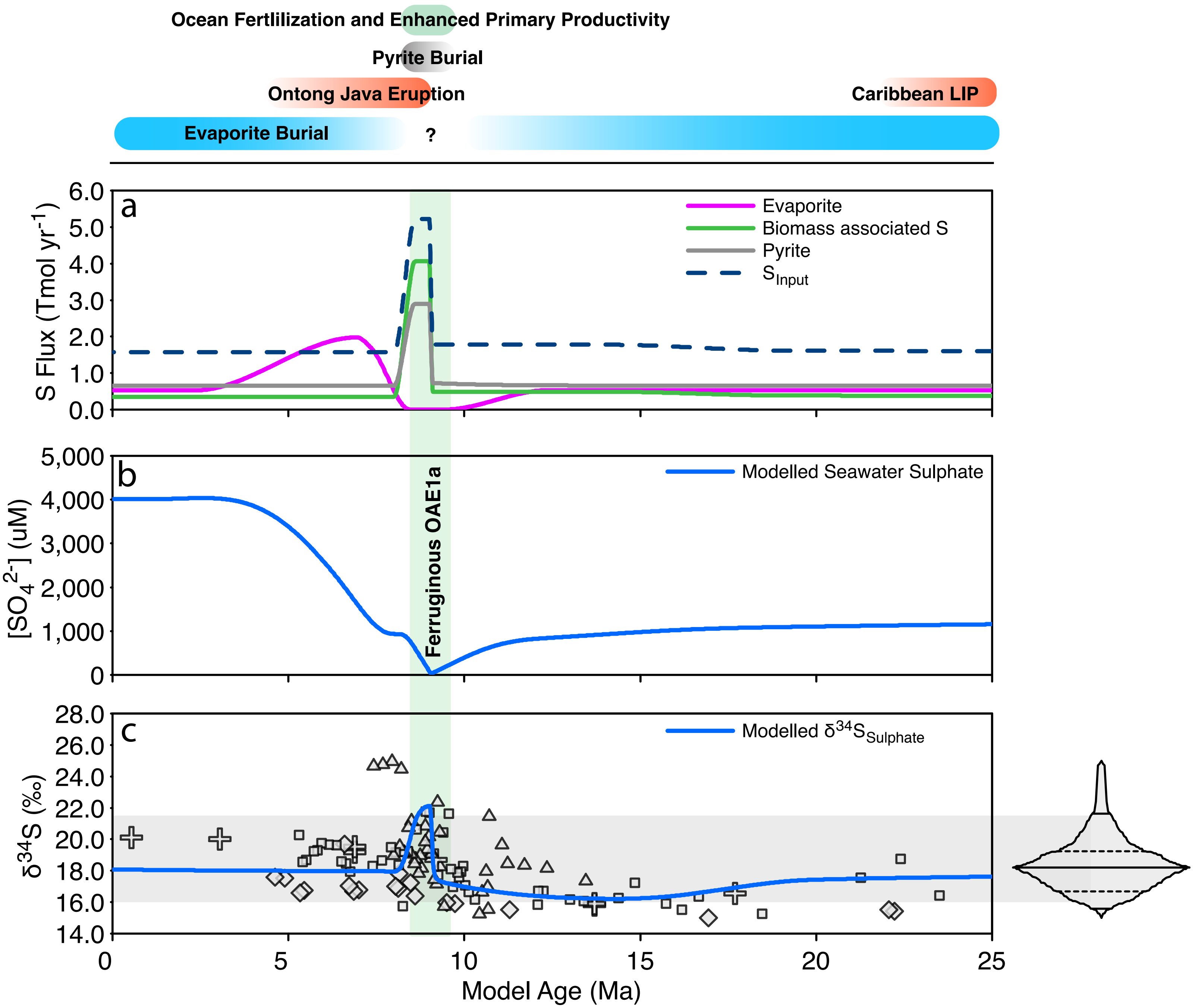
Ocean Fertlilization and Enhanced Primary Productivity
Pyrite Burial
Ontong Java Eruption
Caribbean LIP
Evaporite Burial
?
a
S Flux (Tmol yr$^{-1}$)
6.0
5.0
4.0
3.0
2.0
1.0
0.0
Evaporite
Biomass associated S
Pyrite
$S_{Input}$
b
$[SO_4^{2-}]$ (uM)
5,000
4,000
3,000
2,000
1,000
0
Modelled Seawater Sulphate
Ferruginous OAE1a
c
$\delta^{34}S$ (‰)
28.0
26.0
24.0
22.0
20.0
18.0
16.0
14.0
Modelled $\delta^{34}S_{Sulphate}$
0
5
10
15
20
25
Model Age (Ma)